Proceedings of the ASME 2010 29th International Conference on Ocean, Offshore and Arctic Engineering
OMAE2010
June 6-11, 2010, Shanghai, China

OMAE2010-20613

MECHANISTIC STUDY OF UPPER OCEAN TURBULENCE INTERACTING WITH SURFACE WAVES

Xin Guo, Di Yang, Yi Liu, and Lian Shen*
Department of Civil Engineering
Johns Hopkins University
Baltimore, Maryland 21218
Email: LianShen@jhu.edu

ABSTRACT

We perform direct numerical simulations to simulate the interaction between surface waves and the turbulence underneath. The Navier–Stokes equations are simulated using a pseudo-spectral method in horizontal directions and a finite-difference method in vertical direction, with fully nonlinear viscous free-surface kinematic and dynamic boundary conditions at the free surface. We set up the turbulence and the waves by a random forcing method in the bulk flow and a pressure forcing method at the surface, which were recently developed by [1]. It is found that there are surface waves generated on the free surface due to the excitation by the turbulence. The surface elevation is sensitive to the effect of gravity and surface tension. In the presence of progressive waves at the free surface, the turbulent vortical structure is turned, stretched, and compressed periodically by the strain field of waves.

INTRODUCTION

Wave–turbulence interaction in the upper ocean is important to many applications, including gas and heat transfer at the ocean surface, mixing in the upper layer ocean, and wave evolution. Previous studies [2] showed that gravity waves enhance the turbulence. Analysis of the distortion of waves on turbulence using rapid distortion theory (RDT) [3] showed that turbulence Reynolds stress and vorticity are wave phase dependent. The accumulated effect of the Stokes drift associated with the waves is one of the possible mechanisms that turns vertical vorticity into the streamwise direction. The theoretical analysis also showed that there is direct energy transport between the surface waves and the turbulence. Such energy transport was also observed in experiments [4, 5].

Numerical study of the wave–turbulence interaction requires proper setup of the wave and turbulence fields in the simulation. Most of the previous numerical studies focused on rigid-lid flows with a mean shear to represent the averaged effect of the Stokes drift of surface waves [6–8]. However, the effect of periodic wave straining is omitted. Recently, Guo and Shen [1] overcame the challenges of setting up progressive waves and turbulence precisely in a numerical tank, with the complex wave–turbulence interaction process in presence. Isotropic turbulence in the bulk flow is generated by a linear random force, which is proportional to the velocity fluctuation [9, 10]. The turbulence is then transported and diffused to the near surface region and interacts with the free surface. The progressive wave is generated and maintained by a surface pressure. The results in [1] showed that the progressive wave is well maintained and spurious standing waves are suppressed effectively.

In this study, we perform direction numerical simulation (DNS) of wave–turbulence interaction with the wave and turbulence controlled precisely. Fully nonlinear kinematic and dynamic free-surface boundary conditions (see e.g., [11–13]) are used in our simulation. We study the surface deformation caused by the turbulence underneath. We also study the vortex turning, stretching, and compressing associated with the surface wave.

*Address all correspondence to this author.

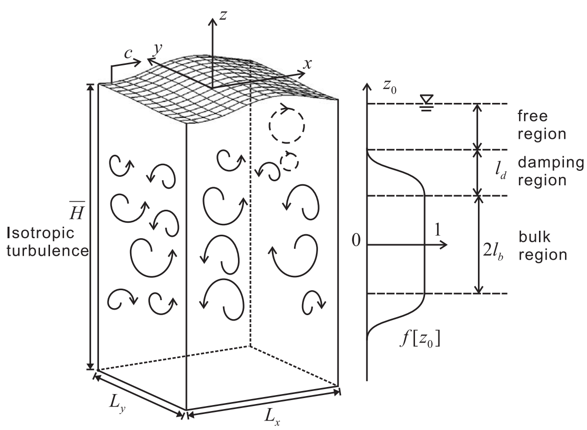

Figure 1. SCHEMATICS OF ISOTROPIC HOMOGENEOUS TURBULENCE INTERACTING WITH A PROGRESSIVE WAVE.

PROBLEM DEFINITION AND NUMERICAL METHOD

We consider direct numerical simulation of a three dimensional turbulent flow under a free surface. As shown in Fig. 1 and below, isotropic turbulence is generated by a body force in the bulk flow, which is different from most of the previous simulations of free-surface turbulence wherein turbulence was generated by the shear at the bottom, the shear in the bulk flow, or initially-seeded turbulence. The region above the free surface is vacuum. The numerical details of wave and turbulence generation are provided in [1]. The present problem setting has a potential to correspond the experiments of interaction between a free surface and homogeneous turbulence generated by oscillating grid or random jets.

In this study, the frame of reference has axes x, y, and z (also denoted as x_1, x_2, and x_3 if tensor notation is used), with x and y horizontal and z vertical. The $+z$ points upward, with the $z=0$ plane coinciding with the undisturbed free surface.

The flow is governed by the incompressible Navier–Stokes equations

$$\frac{\partial u_i}{\partial t}+\frac{\partial\left(u_i u_j\right)}{\partial x_j}=-\frac{\partial p}{\partial x_i}+\frac{1}{\Re}\frac{\partial^2 u_i}{\partial x_j \partial x_j}+a_0 f\left[z_0\right] u_i, \tag{1}$$

$$\frac{\partial u_i}{\partial x_i}=0. \tag{2}$$

Here and hereafter, unless otherwise indicated, all variables are normalized by a characteristic length scale L and a characteristic velocity scale U. The dynamic pressure p is normalized by ρU^2, where ρ is the density of the fluid. The Reynolds number is defined as $\Re = UL/\nu$, with ν the kinematic viscosity. The last term on the right hand side of Eqn. (1) is the body force, which generates homogeneous turbulence in the simulation. The a_0 is the body force parameter at the center of the computational domain; and $f[z_0]$ is the body force distribution function and it varies with z_0, the distance to the center of the computational domain, according to

$$f\left[z_0\right]=\begin{cases}1 & z_0 \le l_b, \\ \frac{1}{2}\left(1-\cos\left[\frac{\pi}{l_d}\left(z_0-l_b-l_d\right)\right]\right) & l_b<z_0\le l_b+l_d, \\ 0 & z_0>l_b+l_d,\end{cases} \tag{3}$$

where l_b is half of the vertical length of the bulk region and l_d is the length of the damping region (Fig. 1) [1].

At the free surface, the kinematic boundary condition (KBC) is

$$\frac{\partial \eta}{\partial t}+u\frac{\partial \eta}{\partial x}+v\frac{\partial \eta}{\partial y}-w=0, \qquad \text{at} \qquad z=\eta. \tag{4}$$

Here η is the elevation of the free surface. The dynamic boundary conditions (DBC's) are

$$\vec{t}_1\cdot[\sigma]\cdot\vec{n}^T=0, \tag{5}$$

$$\vec{t}_2\cdot[\sigma]\cdot\vec{n}^T=0, \tag{6}$$

$$\vec{n}\cdot[\sigma]\cdot\vec{n}^T=\frac{1}{We}\left(\frac{1}{R_1}+\frac{1}{R_2}\right). \tag{7}$$

In the above equations, the stress tensor $[\sigma]$ is expressed as

$$\sigma_{ij}=-P\delta_{ij}+\frac{1}{\Re}\left(\frac{\partial u_i}{\partial x_j}+\frac{\partial u_j}{\partial x_i}\right), \tag{8}$$

where δ_{ij} is the Kronecker delta. Here $P=p-z/Fr^2$, where the Froude number is defined as $Fr=U/\sqrt{gL}$, with g the gravitational acceleration. And $\vec{n}$ is the unit vector normal to the free surface pointing from the fluid to the vacuum; $\vec{t}_1$ and $\vec{t}_2$ are unit vectors tangential to the free surface. They are expressed as

$$\vec{n}=\frac{(-\eta_x,-\eta_y,1)}{\sqrt{\eta_x^2+\eta_y^2+1}}, \quad \vec{t}_1=\frac{(1,0,\eta_x)}{\sqrt{\eta_x^2+1}}, \quad \vec{t}_2=\frac{(0,1,\eta_y)}{\sqrt{\eta_y^2+1}}. \tag{9}$$

In Eqn. (7), $We=\rho U^2 L/\gamma$ is the Weber number, with γ the surface tension coefficient; and $1/R_1$ and $1/R_2$ are the principal curvatures of the surface that satisfy

$$\frac{1}{R_1}+\frac{1}{R_2}=\frac{\left(1+\eta_x^2\right)\eta_{yy}+\left(1+\eta_y^2\right)\eta_{xx}-2\eta_x\eta_y\eta_{xy}}{\left(1+\eta_x^2+\eta_y^2\right)^{3/2}}. \tag{10}$$

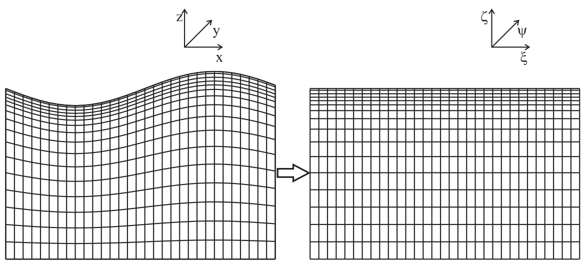

Figure 2. SKETCH PLOT OF THE ALGEBRAIC MAPPING THAT TRANSFORMS THE IRREGULAR CARTESIAN SPACE (x,y,z,t) CONFINED BY THE FREE SURFACE TO A RECTANGULAR COMPUTATIONAL DOMAIN $(\xi,\psi,\varsigma,\tau)$.

At the bottom $z=-\overline{H}$, free-slip boundary condition is imposed. In horizontal directions, periodic boundary condition is applied.

In the simulation of free-surface turbulence, a major issue is that the shape of the surface is irregular and time-dependent. In this study, we employ a boundary-fitted grid to simulate Eqns. (1) and (2) subject to Eqns. (4), (5), (6), and (7). The irregular space (x,y,z,t) confined by the free surface is transformed to a rectangular computational domain $(\xi,\psi,\varsigma,\tau)$ by an algebraic mapping, which is similar to the 2-D σ-transform used in the previous studies [14, 15], defined as [1]

$$\tau=t,\quad \xi=x,\quad \psi=y,\quad \varsigma=\frac{z+\overline{H}}{\eta+\overline{H}}. \tag{11}$$

We normalize the vertical dimension by $\eta+\overline{H}$. The grid is stretched in the vertical direction. A sketch plot of the mapping is shown in Fig. 2. We note that conformal mapping is often preferred for flow simulations in complex geometries (see e.g. [11]). In the present problem, because the surface slope is not large, the grid distortion associated with the algebraic mapping (11) has a negligible effect on the simulation accuracy. Therefore, we chose the current algebraic mapping for simplicity, which can save computational cost greatly. As shown in [1], the effect of computational grid distortion due to the algebraic mapping on turbulence is negligible.

With Eqn. (11), based on the chain rule, we have

$$\begin{cases} \dfrac{\partial}{\partial t}=\dfrac{\partial}{\partial\tau}-\dfrac{\varsigma\eta_t}{\eta+\overline{H}}\dfrac{\partial}{\partial\varsigma}, \\ \dfrac{\partial}{\partial x}=\dfrac{\partial}{\partial\xi}-\dfrac{\varsigma\eta_x}{\eta+\overline{H}}\dfrac{\partial}{\partial\varsigma}, \\ \dfrac{\partial}{\partial y}=\dfrac{\partial}{\partial\psi}-\dfrac{\varsigma\eta_y}{\eta+\overline{H}}\dfrac{\partial}{\partial\varsigma}, \\ \dfrac{\partial}{\partial z}=\dfrac{1}{\eta+\overline{H}}\dfrac{\partial}{\partial\varsigma}. \end{cases} \tag{12}$$

Therefore, we obtain expressions for Eqns. (1) and (2) in the new coordinate system as

$$\begin{aligned} &\frac{\partial u}{\partial\tau}+\frac{\partial p}{\partial\xi}-\frac{\varsigma\eta_x}{\eta+\overline{H}}\frac{\partial p}{\partial\varsigma} \\ &=-\frac{\partial(uu)}{\partial\xi}-\frac{\partial(uv)}{\partial\psi}-\frac{1}{\eta+\overline{H}}\frac{\partial(uw)}{\partial\varsigma} \\ &\quad+\frac{\varsigma}{\eta+\overline{H}}\left[\eta_t\frac{\partial u}{\partial\varsigma}+\eta_x\frac{\partial(uu)}{\partial\varsigma}+\eta_y\frac{\partial(uv)}{\partial\varsigma}\right]+\frac{1}{\Re}\nabla^2u, \end{aligned} \tag{13}$$

$$\begin{aligned} &\frac{\partial v}{\partial\tau}+\frac{\partial p}{\partial\psi}-\frac{\varsigma\eta_y}{\eta+\overline{H}}\frac{\partial p}{\partial\varsigma} \\ &=-\frac{\partial(uv)}{\partial\xi}-\frac{\partial(vv)}{\partial\psi}-\frac{1}{\eta+\overline{H}}\frac{\partial(vw)}{\partial\varsigma} \\ &\quad+\frac{\varsigma}{\eta+\overline{H}}\left[\eta_t\frac{\partial v}{\partial\varsigma}+\eta_x\frac{\partial(vu)}{\partial\varsigma}+\eta_y\frac{\partial(vv)}{\partial\varsigma}\right]+\frac{1}{\Re}\nabla^2v, \end{aligned} \tag{14}$$

$$\begin{aligned} &\frac{\partial w}{\partial\tau}+\frac{1}{\eta+\overline{H}}\frac{\partial p}{\partial\varsigma} \\ &=-\frac{\partial(wu)}{\partial\xi}-\frac{\partial(wv)}{\partial\psi}-\frac{1}{\eta+\overline{H}}\frac{\partial(ww)}{\partial\varsigma} \\ &\quad+\frac{\varsigma}{\eta+\overline{H}}\left[\eta_t\frac{\partial w}{\partial\varsigma}+\eta_x\frac{\partial(wu)}{\partial\varsigma}+\eta_y\frac{\partial(wv)}{\partial\varsigma}\right]+\frac{1}{\Re}\nabla^2w, \end{aligned} \tag{15}$$

and

$$\frac{\partial u}{\partial\xi}-\frac{\varsigma\eta_x}{\eta+\overline{H}}\frac{\partial u}{\partial\varsigma}+\frac{\partial v}{\partial\psi}-\frac{\varsigma\eta_y}{\eta+\overline{H}}\frac{\partial v}{\partial\varsigma}+\frac{1}{\eta+\overline{H}}\frac{\partial w}{\partial\varsigma}=0. \tag{16}$$

The operator ∇^2 in Eqns. (13)–(15) and the free-surface boundary conditions (4)–(7) are also expressed in terms of $(\xi, \psi, \varsigma, \tau)$.

For space discretization, in ξ and ψ directions, we use a pseudo-spectral method with Fourier series; in ς direction, we use a second-order finite-difference scheme on a staggered grid [16]. The numerical scheme we use is based on the fractional-step method discussed in [17]. We use a second-order Crank–Nicholson scheme for the viscous terms and a second-order Adams–Bashforth scheme for the convection terms. The surface elevation is advanced in time with a second-order Runge–Kutta scheme. We note that explicit numerical schemes were often used in the literature when solving the momentum equation for the study of the interaction between laminar flows and free surfaces [13, 18, 19]. For the present DNS study of turbulent flows, however, a much higher spatial resolution is required to resolve the fine turbulence structures in three dimension. If an explicit scheme is used, the small grid size leads to small time steps and thus high computational cost. The semi-implicit Crank–Nicholson scheme used in the current study allows us to use relatively large time steps with fine grids.

Our computational domain size is $L_x \times L_y \times \overline{H} = 2\pi \times 2\pi \times 5\pi$. We set $\Re$ and a_0 to be 1000 and 0.1, respectively. Based on Eqns. (36) and (38) in [1], the velocity fluctuation at the center of the free region (Fig. 1) u^{rms} is 0.090 and the Taylor scale λ is 0.339. Therefore, the Taylor-scale Reynolds number is $\Re_\lambda = u^{rms}\lambda/\nu = 30.39$ near the free surface. We use a $128 \times 128 \times 348$ grid. In horizontal directions, the grids are evenly distributed. In the vertical direction, the grids are clustered towards the free surface; there are about 60 points in the free region and 10 points in the viscous layer of the free surface to ensure the boundary layer at the free surface is resolved adequately.

We note that in [13] and [20], adaptive grids were used in both the horizontal and vertical directions when studying the interaction of vortex pair with a free surface. The adaptive grids allow the resolution of the detailed flow structure near the vortex pair and the free surface with affordable computational cost. In the current study, the grid points are clustered only in the vertical direction with fine grid size near the free surface. In the horizontal directions, evenly-spaced grid is used together with a Fourier-series-based spectral method. The strategy of the present simulation is determined by the nature of the problem being studied: the turbulence near the free surface has a fine surface layer structure in the surface-normal direction, while in the surface-tangential directions a continuous turbulence energy spectrum exists (see e.g., Fig. 3).

RESULTS

In this section, we discuss the simulation results of two canonical problems: the interaction of isotropic and homogeneous turbulence (IHT) with a deformable surface (hereinafter referred to as 'Problem I'), and the distortion of IHT by a progressive surface wave (hereinafter referred to as 'Problem II').

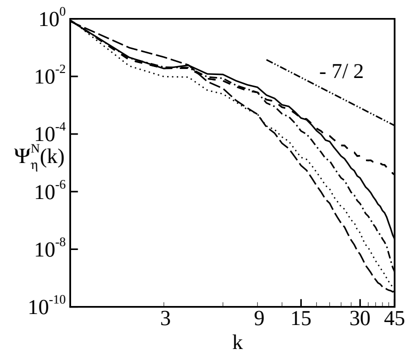

Figure 3. NORMALIZED SURFACE ELEVATION SPECTRA FOR: —— , ($Fr^2 = 0.1$, $We^{-1} = 0.025$); – – – , ($Fr^2 = 0.2$, $We^{-1} = 0$); – · – · – , ($Fr^2 = 0.2$, $We^{-1} = 0.025$); · · · · · · , ($Fr^2 = 0.2$, $We^{-1} = 0.05$); —— , ($Fr^2 = 0.8$, $We^{-1} = 0.025$).

Problem I: Surface Elevation Spectrum

In the simulation of Problem I, the surface is initially calm and the IHT is generated at certain distance beneath the free surface [1]. When the coherent turbulence structures transport and diffuse to the free surface boundary layer, they interact with the deformable surface and have significant effect on the surface geometry. The significance of such interaction is controlled by the relative intensity of the turbulence with respect to the surface restoring forces due to gravity and surface tension, which are characterized by the Froude and Weber numbers, respectively.

We first examine the spectrum of the surface elevation and its dependence on the Froude and Weber numbers. Because the current problem is isotropic in the horizontal directions, a one-dimensional spatial spectrum for $\eta(\vec{x}, t)$ can be defined as

$$\Psi_\eta\left(\left|\vec{k}\right|\right) = \frac{1}{(2\pi)^2}\int_S \overline{\eta\left(\vec{x},t\right)\eta\left(\vec{x}+\vec{r},t\right)} \cdot \mathrm{e}^{-\mathrm{i}\vec{k}\cdot\vec{r}}\,\mathrm{d}\vec{r}. \qquad (17)$$

Here $\vec{x}$ and $\vec{r}$ refer to horizontal vectors. The spectrum is normalized as

$$\Psi^N_\eta\left(\left|\vec{k}\right|\right) = \frac{\Psi_\eta\left(\left|\vec{k}\right|\right)}{(\eta^{rms})^2}. \qquad (18)$$

Here η^{rms} denotes the root-mean-square value of η with the statistics performed first in the horizontal directions and then in time. Figure 3 plots Ψ^N_η for different (Fr^2, We^{-1}) cases. The surface elevation increases monotonically as k decreases, because the underlying homogeneous turbulence excited by the random force has the largest energy at $k=1$ [10]. At large k, the case without surface tension ($Fr^2=0.2$, $We^{-1}=0$) has an η spectrum proportional to $k^{-7/2}$. For the other cases shown in Fig. 3, the surface tension effect becomes important at large wavenumbers.

The relative importance of the gravity and surface tension effects can be measured by a critical wavenumber suggested by [21], which is defined as

$$k_{cr}=\sqrt{\frac{We}{Fr^2}}. \tag{19}$$

The physical meaning of k_{cr} can be understood through a simple model for a monochromatic wave with wavenumber k and small amplitude a_k. The density of gravitational potential energy is

$$E_{p,g}\approx\frac{1}{4}\frac{a_k^2}{Fr^2}. \tag{20}$$

The density of the surface tension potential energy is

$$\begin{aligned}E_{p,\gamma}&\approx We^{-1}\cdot\frac{1}{2S}\int_S\left[\left(\frac{\partial\eta}{\partial x}\right)^2+\left(\frac{\partial\eta}{\partial y}\right)^2\right]\mathrm{d}x\,\mathrm{d}y\\&=\frac{1}{4}We^{-1}k^2a_k^2.\end{aligned} \tag{21}$$

Therefore, the ratio between the two types of potential energy is

$$\frac{E_{p,\gamma}}{E_{p,g}}\approx We^{-1}Fr^2k^2=\left(\frac{k}{k_{cr}}\right)^2. \tag{22}$$

When $k<k_{cr}$, the gravity effect is more important; whereas when $k>k_{cr}$, the surface tension effect dominates.

For $k>k_{cr}$, Ψ_η^N decreases significantly. We note that none of the present cases are purely capillary waves. Therefore, the k^{-5}-scaling [22] does not show here.

The relative importance of gravity and surface tension effects in the spectral space can be seen in Fig. 3. When We^{-1} is fixed and Fr^2 increases, or when Fr^2 is fixed and We^{-1} increases, the surface elevation decreases at large k. According to Eqn. (19), the critical wavenumber k_{cr} decreases. As a result, for $k>k_{cr}$ where the surface tension effect dominates, the surface fluctuation decreases significantly.

In addition to the spatial statistics of surface elevation, we can further investigate its temporal features via the spatial–temporal spectrum

$$\Phi_a\left(\left|\vec{k}\right|,\sigma\right)=\frac{1}{(2\pi)^3}\int_T\int_S\left\{\overline{\eta(\vec{x},t)\,\eta(\vec{x}+\vec{r},t+\tau)}\cdot\mathrm{e}^{-\mathrm{i}\left(\vec{k}\cdot\vec{r}+\sigma\tau\right)}\right\}\mathrm{d}\vec{r}\,\mathrm{d}\tau, \tag{23}$$

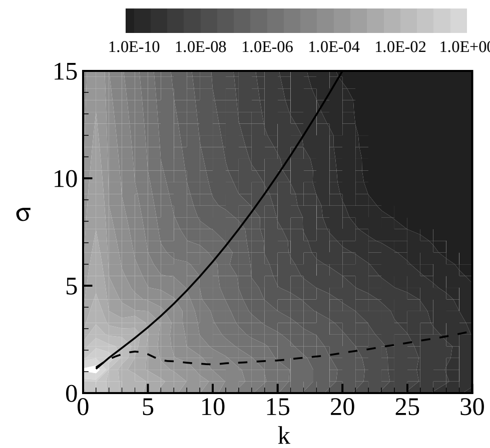

Figure 4. NORMALIZED SPATIAL–TEMPORAL SPECTRUM OF THE SURFACE ELEVATION FOR THE CASE OF ($Fr^2=0.8$, $We^{-1}=0.025$). —— , DISPERSION RELATIONSHIP (25); – – – , CHARACTERISTIC FREQUENCY BASED ON FULLY NONLINEAR KBC (26).

which is normalized as

$$\Phi_a^N\left(\left|\vec{k}\right|,\sigma\right)=\frac{\Phi_a\left(\left|\vec{k}\right|,\sigma\right)}{\left(\eta^{rms}\right)^2}. \tag{24}$$

Figure 4 shows Φ_a^N. For the case of ($Fr^2=0.8$, $We^{-1}=0.025$), energy is concentrated on two ridges in the contour plot, which correspond to two types of surface motions, namely propagating surface waves and turbulence-induced surface deformation. To show the waves, we consider the dispersion relationship for small-amplitude deep-water waves:

$$\sigma_*=\sqrt{\frac{k}{Fr^2}+\frac{k^3}{We}}, \tag{25}$$

which is plotted in Fig. 4 as the solid line. It fits the high-frequency ridge well. The fact that the high-frequency ridge is manifested mainly at small k region suggests that surface waves are of large scales, which is as expected because small-scale waves are quickly damped in the turbulence field.

For the surface deformation associated with the turbulence motion, the characteristic frequency of η at each k is quantified as

$$\sigma_n=\sqrt{\frac{\Psi_\eta(k)}{\Psi_{\eta_t}(k)}}. \tag{26}$$

Equation (26) takes into account the nonlinearity of surface motion ($\eta_t=w-u\eta_x-v\eta_y$). Figure 4 shows that Eqn. (26) fits the

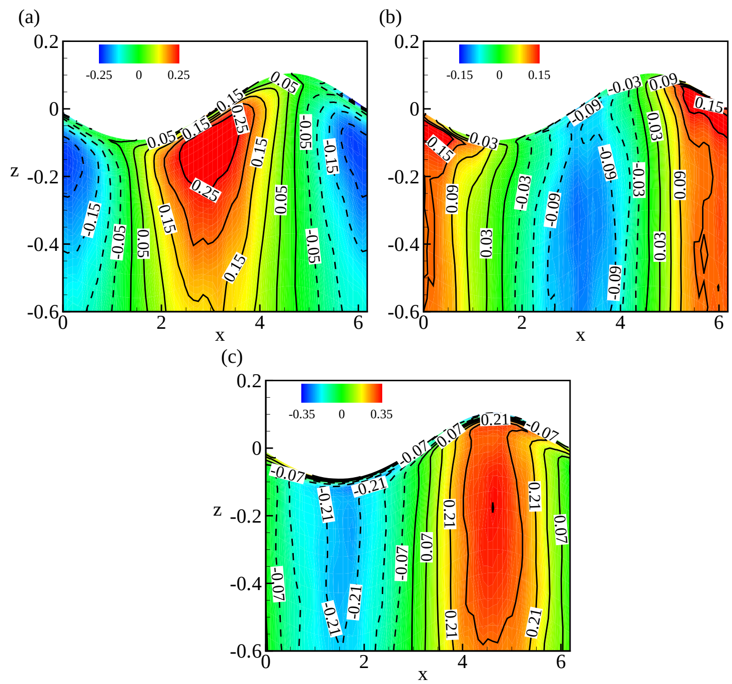

Figure 5. CONTOURS OF (a) $\langle|\omega_x|\partial u/\partial x\rangle$, (b) $\langle|\omega_z|\partial w/\partial z\rangle$, AND (c) $\langle|\omega_z|\partial u/\partial z\rangle$. THE WAVE PROPAGATES FROM LEFT TO RIGHT.

low-frequency ridge. We remark that our results are consistent with the recent experiment by [23].

The result in Fig. 4 shows that the surface motion can be described by the dispersion relationship for surface waves and the nonlinear-KBC based characteristic frequency for turbulence-induced surface deformation. The waves mainly happen at small k. The surface deformation associated with the turbulence, on the other hand, occurs over a wide range of wavenumbers because of the turbulence motions at the corresponding scales. As shown in Fig. 4, at small k, the frequency given by the dispersion relationship is close to the characteristic frequency associated with turbulence, indicating that waves may be excited by turbulence structures at large scales. At large k, there exists large gap between the two frequencies. As a result, small-scale waves are less likely to be generated, and turbulence-induced roughness dominates at large k.

Problem II: Turbulent Vorticity Distribution Under A Surface Wave

We next discuss the influence of a progressive surface wave on the underlying turbulence vorticity. In our simulation of Problem II, one progressive surface wave, which propagates in $+x$-direction, is generated and maintained to provide a continuous distorting strain field to the IHT field. In the transverse direction, periodic boundary condition is applied. Therefore, the flow is quasi-three-dimensional. From the instantaneous flow field (not shown here), we observe that vortices are stretched and turned by the wave motion. Our statistical results confirm this observation. Among the different terms in the vortex dynamics equation [24], we found that vortex stretching plays an important role in the evolution of $\langle\omega_x\rangle$ and $\langle\omega_z\rangle$ (variation in $\langle\omega_y\rangle$ is small and is thus not a focus here). Figures 5(a) and (b) show the distributions of the vortex stretching terms $\langle|\omega_x|\partial u/\partial x\rangle$ and $\langle|\omega_z|\partial w/\partial z\rangle$, respectively. Here the absolute value is used because for both positive and negative ω_x and ω_z, the same mechanism exists; averaging without the absolute value results in cancelation in the statistical value.

For the streamwise vortices, Fig. 5(a) shows that $\langle|\omega_x|\partial u/\partial x\rangle$ is positive under the backward face of the wave and negative under the forward face of the wave. When the backward face of the wave passes by, streamwise vortices are stretched. As a result, $\langle\omega_x'^2\rangle$ reaches its maximum value under the wave trough. Compression occurs when the forward face of the wave passes by. Therefore, $\langle\omega_x'^2\rangle$ reaches its minimum value under the wave crest. For the vertical vorticity, Fig. 5(b) shows that $\langle|\omega_z|\partial w/\partial z\rangle$ is positive under the forward face of the wave and negative under the backward face of the wave, which leads to the maximum value in $\langle\omega_z'^2\rangle$ under the wave crest and minimum value under the wave trough.

It is found that vortex turning also plays an important role in the evolution of vertical vorticity. The vortex turning term $\langle|\omega_z|\partial u/\partial z\rangle$ is plotted in Fig. 5(c). Due to the wave orbital motion, near the surface, vertical vortices are turned to the wave propagating direction under the forward face of the wave crest and the backward face of the wave trough, and to the opposite direction under the forward face of the wave trough and the backward face of the wave crest. As a result, $\langle|\omega_z|\partial u/\partial z\rangle$ has positive–negative staggered distribution as shown in Fig. 5(c). However, this vortex turning term under the forward face of the wave crest is much stronger than at other places. Therefore, the net effect is that vertical vortices are turned to the streamwise direction. This result is consistent with the analysis of the Stokes drift by [3]. Finally, we remark that because the vortex turning and stretching terms are highly phase dependent, the configuration of vortical structures are in general quite complex.

CONCLUSION

In this work, we have used direct numerical simulation technique to study the interaction of isotropic homogeneous turbulence with a deformable free surface and progressive surface waves. Our simulation captures the detailed structures in the flow. The surface elevation signature agrees with the existing free surface wave and turbulence theories and experimental observations. Our statistical analysis on wave–turbulence interaction has also revealed unique features of turbulence vortical structures under the influence of the progressive surface wave field. The turbulence vorticity is strongly wave-phase dependent due to the stretching and compressing by the strain field of the surface wave. The vertical vortex is turned to the streamwise direction by the accumulated effect of the surface wave. Further systematic investigation and more detailed discussion on this topic will be reported in our future work.

ACKNOWLEDGMENT

We would like to thank the referees for their valuable comments that provide us help to improve the previous version of this paper.

REFERENCES

[1] Guo, X., and Shen, L., 2009. "On the generation and maintenance of waves and turbulence in simulations of free-surface turbulence". *Journal of Computational Physics,* ***228***, pp. 7313–7332.

[2] Phillips, O. M., 1961. "A note on the turbulence generated by gravity waves". *Journal of Geophysical Research,* ***66***, pp. 2889–2893.

[3] Teixeira, M. A. C., and Belcher, S. E., 2002. "On the distortion of turbulence by a progressive surface wave". *Journal of Fluid Mechanics,* ***458***, pp. 229–267.

[4] Jiang, J.-Y., and Street, R. L., 1991. "Modulated flows beneath wind-ruffled, mechanically generated water waves". *Journal of Geophysical Research,* ***96***, pp. 2711–2721.

[5] Thais, L., and Magnaudet, J., 1996. "Turbulent structure beneath surface gravity waves sheared by the wind". *Journal of Fluid Mechanics,* ***328***, pp. 313–344.

[6] McWilliams, J. C., Sullivan, P. P., and Moeng, C.-H., 1997. "Langmuir turbulence in the ocean". *Journal of Fluid Mechanics,* ***334***, pp. 1–30.

[7] Li, M., Garrett, C., and Skyllingstad, E., 2005. "A regime diagram for classifying turbulent large eddies in the upper ocean". *Deep-sea Research A,* ***52***, pp. 259–278.

[8] Polton, J. A., and Belcher, S. E., 2007. "Langmuir turbulence and deeply penetrating jets in an unstratified mixed layer". *Journal of Geophysical Research,* ***112***, p. C09020.

[9] Lundgren, T., 2003. Linearly forced isotropic turbulence. Annual Research Briefs 461, Center for Turbulence Research, Standford, CA.

[10] Rosales, C., and Meneveau, C., 2005. "Linear forcing in numerical simulations of isotropic turbulence: Physical space implementations and convergence properties". *Physics of Fluids,* ***17***, p. 095106.

[11] Yeung, R. W., 1991. "Nonlinear bow and stern waves - inviscid and viscous solutions". In *Mathematical Approaches in Hydrodynamics*, T. Miloh, ed. SIAM Publisher, May, Chapter 24, pp. 349–369.

[12] Dommermuth, D. G., 1993. "The laminar interactions of a pair of vortex tubes with a free surface". *Journal of Fluid Mechanics,* ***246***, pp. 91–115.

[13] Ananthakrishnan, P., and Yeung, R. W., 1994. "Nonlinear interaction of a vortex pair with clean and surfactant-covered free surfaces". *Wave Motion,* ***19***, pp. 343–365.

[14] Turnbull, M. S., Borthwick, A. G. L., and Taylor, R. E., 2003. "Numerical wave tank based on a σ-transformed finite element inviscid flow solver". *International Journal for Numerical Methods in Fluids,* ***42***, pp. 641–663.

[15] Frandsen, J. B., and Borthwick, A. G. L., 2003. "Simulation of sloshing motions in fixed and vertically excited containers using a 2-d inviscid σ-transformed finite difference solver". *Journal of Fluids and Structures,* ***18***, pp. 197–214.

[16] Harlow, F. H., and Welch, J. E., 1965. "Numerical calculation of time-dependent viscous incompressible flow of fluid with free surface". *Physics of Fluids,* ***8***, pp. 2182–2189.

[17] Kim, J., and Moin, P., 1985. "Application of a fractional-step method to incompressible Navier–Stokes equations". *Journal of Computational Physics,* ***59***, pp. 308–323.

[18] Yeung, R. W., and Vaidhyanathan, M., 1992. "Non-linear interaction of water waves with submerged obstacles". *International Journal for Numerical Methods in Fluids,* ***14***, pp. 1111–1130.

[19] Zhang, C., Shen, L., and Yue, D. K. P., 1999. "The mechanism of vortex connection at a free surface". *Journal of Fluid Mechanics,* ***384***, pp. 207–241.

[20] Ohring, S., and Lugt, H. J., 1991. "Interaction of a viscous vortex pair with a free surface". *Journal of Fluid Mechanics,* ***227***, pp. 47–70.

[21] Phillips, O. M., 1958. "The equilibrium range in the spectrum of wind-generated waves". *Journal of Fluid Mechanics,* ***4***, pp. 426–434.

[22] Lleonart, G. T., and Blackman, D. R., 1980. "The spectral characteristics of wind-generated capillary waves". *Journal of Fluid Mechanics,* ***97***, pp. 455–479.

[23] Savelsberg, R., and Van de Water, W., 2009. "Experiments on free-surface turbulence". *Journal of Fluid Mechanics,* ***619***, pp. 95–125.

[24] Yang, D., and Shen, L., 2009. "Characteristics of coherent vortical structures in turbulent flows over progressive surface waves". *Physics of Fluids,* ***21***, p. 125106.